Supporting Appendix

Supplementary notes

Note 1: The Turing Model of pattern formation.

Diffusion-driven instability is a canonical mechanism invoked to explain the emergence of space-filling patterns from an initially homogeneous condition (1-3). In the simplest case, the system is constituted of two diffusible and reactive substances (the morphogens). One of them is an activator; it stimulates the production of itself as well as its antagonist, the inhibitor. The inhibitor represses the production of the activator. Both the activator and the inhibitor have finite life times. It was pointed out by Turing (2) that a homogeneous state of this system is unstable, in the sense that any random fluctuation will get amplified and develop into spatially structured patterns, if certain criteria of the kinetic properties of the morphogens are satisfied. These criteria are commonly known as "short-range activation and long-range inhibition". Typically, they are realized by having activators that are either short lived and/or slow diffusing (or inhibitors that are long lived and/or fast diffusing), such that the synthesis of activators and inhibitors only occur in localized neighborhoods (e.g., spots or stripes). The exact location of spots or stripes depends on small fluctuations in the activator and inhibitor concentrations in the initial condition, and is typically not predictable in advance.

Note 2: The Expansion-Induction Model.

The simplest formulation of the EI model is for a single diffusing inhibitor and basal activation (Fig. 2*B*). We give a continuum formulation here for the sake of compactness. The discrete numerical implementation is given in the Supplementary Methods section (below).

Let the concentration of the inhibitor in the two-dimensional space $\bar{r} \in (x,y)$ be $R(\bar{r},t)$, with diffusion coefficient D_R, turnover rate μ_R. Then, the temporal evolution of the inhibitor field is described by the following equation

$$\frac{\partial R(\bar{r},t)}{\partial t} = D_R \nabla^2 R(\bar{r},t) - \mu_R R(\bar{r},t) + \gamma_R (\bar{r},t) - \nabla \cdot (R(\bar{r},t)\bar{v}(\bar{r},t)) \qquad (1)$$

where $\gamma_R(\vec{r},t)$ is the inhibitor synthesis rate. We assume inhibitor synthesis is localized to the positions of the existing follicles. Let the position of the nth follicle be $\vec{r}_n$ and its birth time be t_n, then the inhibitor synthesis function is given by

$$\gamma_R(\vec{r},t) = \gamma_{R,0} \cdot a^2 \cdot \sum_{n=1}^{N(t)} \delta(\vec{r}(t) - \vec{r}_n(t)), \tag{2}$$

where δ is the Dirac delta function, $N(t)$ is the total number of follicles at time t, a is a microscopic cutoff length (spatial resolution), and γ_{R0} is the rate of inhibitor synthesis by one follicle, assumed to be the same for all follicles regardless of their birth time.

Tissue dilation is included in the changing locations of the follicles, and in the final term in Eq. (2), which gives dilution and convection due to expansion. Dilation is easier to understand if Eq. (2) is made dimensionless. The range of the diffusible inhibitor sets the length scale of the problem:

$$X_R = \sqrt{D_R / \mu_R}. \tag{3}$$

The relevant time scale is

$$T_0 = 1 / \varepsilon, \tag{4}$$

where ε is the tissue expansion rate; and the concentration scale is

$$R_0 = \gamma_{R,0} a^2 / D_R. \tag{5}$$

This is the peak inhibitor concentration at the follicle, set by the balance of the local synthesis rate and diffusion of the inhibitors. The dimensionless equation is then

$$\left(\frac{\varepsilon}{\mu_R}\right)\left(\frac{\partial \tilde{R}}{\partial t} + \nabla \cdot \left(\tilde{v}\tilde{R}\right)\right) = \nabla^2 \tilde{R} - \tilde{R} + \sum_{n=1}^{N(\tilde{t})} \delta\left(\tilde{\vec{r}}(\tilde{t}) - \tilde{\vec{r}}_n(\tilde{t})\right), \tag{6}$$

where $\tilde{R}(\tilde{\vec{r}},\tilde{t}) = R(\vec{r},t) / R_0$, $\tilde{\vec{r}} = \vec{r} / X_R$, $\tilde{t} = \varepsilon t$, $\tilde{\vec{v}} = \vec{v} / X_R \varepsilon$. In the following equations, the tilde has been dropped for clarity. If we make the reasonable assumption that $\mu_R \gg \varepsilon$, i.e., the diffusion of the morphogens occur at a much faster time scale than tissue expansion, then we need only to solve

$$\nabla^2 R - R + \sum_{n=1}^{N(\tilde{t})} \delta\left(\tilde{\vec{r}}(\tilde{t}) - \tilde{\vec{r}}_n(\tilde{t})\right) = 0 \tag{7}$$

to find $R(\vec{r},t)$ at each time point. In cases where the expansion rate and turnover rate are more similar, the full reaction diffusion equation may be solved using standard numerical approaches. This form of the equation permits a simple solution in the form of a sum over $G\left(\vec{r}\,|\,\vec{r}_n\right)$ for each follicle position, $\vec{r}_n(t)$:

$$R(\vec{r},t) = \sum_{n=1}^{N(t)} G\left(\vec{r}\,|\,\vec{r}_n(t)\right), \quad G\left(\vec{r}\,|\,\vec{r}_n\right) = \frac{K_0\left(|\vec{r} - \vec{r}_n|\right)}{2} \tag{8}$$

where $G\left(\vec{r}\,|\,\vec{r}_n\right)$, the Green's function of Eq. (7), is the second modified Bessel function, indicated by K_0 above.

The tissue expansion manifests in Eq. (7) through the changing follicle positions $\vec{r}_n(t)$; however, it is actually most easily implemented numerically by having fixed follicle locations, changing instead the extinction length l_R of the Green's function with growth. In this case:

$$G(\vec{r}\,|\,\vec{r}_n,t) = \frac{1}{2}K_0\left(\frac{|\vec{r} - \vec{r}_n|}{l_R(t)}\right), \quad l_R = \frac{X_R}{1+t}. \tag{9}$$

Expansion causes the inhibitor concentration to decrease everywhere. To generate new follicles, we impose the rule that if the inhibitor concentration at some point $\vec{r}^*$ drops to a threshold level R^* at time t^*, then, a new follicle is created at position $\vec{r}^*$ with birth time being t^*, i.e.,

$$\begin{array}{l} N(t^*) = N(t^* - \delta t) + 1 \\ \text{with } \vec{r}_{N(t^*)} = \vec{r}^*,\ t_{N(t^*)} = t^* \end{array} \quad \text{if } R(\vec{r}^*,t^*) \le R^* \tag{10}$$

The newly created follicles immediately contribute to the synthesis of inhibitors according to Eq. (2), such that no more follicles are created in the immediate vicinity of $\vec{r}^*$. This rule simulates the action of a basal level of activator for follicle induction, which is suppressed by the inhibitor until it falls below the threshold. Within our model, this threshold (in dimensionless units) represents the only chemical parameter that can affect the pattern secondary follicles formed relative to the primary follicles. The reaction-diffusion and growth parameters are

necessary only if the absolute spatial and temporal dimensions are desired, in which case they can be constrained through fits to the data.

In the discrete simulation of the above system (described in Supplementary Methods), a finite δt means that there is often an extended region in space where the condition $R(\vec{r}^{*},t^{*}) \leq R^{*}$ is satisfied. To choose new follicle locations without taking too small a time step, we first place a follicle at the global minimum of $R(\vec{r},t) < R^{*}$. The inhibitor concentration is recalculated with the new follicle, and the procedure is repeated until R is everywhere above the threshold. At this point, time is advanced again.

Finally, the EI model does not require there be only a diffusible inhibitor with a constant level of (basal) activation. It can also accommodate the case where the activator is diffusible and synthesized by the existing follicles. The activator concentration $A(\vec{r},t)$ can be determined in the same way as the repressor above. There is a new characteristic length scale $X_A = \sqrt{D_A / \mu_A}$ and production rate $A_0 = \gamma_{A,0} a^2 / D_A$, which appear in the Green's function for the activator

$$G_A(\vec{r}|\vec{r}_n,t) = \frac{A_0}{2R_0} K_0\left(\frac{|\vec{r}-\vec{r}_n|}{l_A}\right), \quad l_A = \frac{X_A}{X_R} l_R . \tag{11}$$

With a diffusible activator, the rule for new follicle formation may be generalized to, e.g.,

$$\begin{aligned} N(t^*) &= N(t^* - \delta t) + 1 \\ \text{with } \vec{r}_{N(t^*)} &= \vec{r}^{*}, \ t_{N(t^*)} = t^{*} \end{aligned} \quad \text{if} \quad \frac{R(\vec{r}^{*},t^{*})}{A(\vec{r}^{*},t^{*})} \leq \theta \tag{12}$$

where θ is the threshold level of the inhibitor-activator ratio. The key criterion for pattern formation in the case of the diffusible activator is that the activator should act over longer range than the inhibitor, i.e.,

$$X_A = \sqrt{D_A / \mu_A} > X_R = \sqrt{D_R / \mu_R} . \tag{13}$$

In the discrete simulation, the new follicle is created at the local minimum of $R(\vec{r},t) / A(\vec{r},t)$.

Note 3: The effect of noggin treatment in explant culture.

Noggin is a homodimeric glycoprotein withe high affinity for Bmp2 and Bmp4 and with varying affinities for Bmp5, Bmp6, Bmp7, GDF5 and GDF6, but apparently not other members of the TGF-β family of peptides (4-6). Noggin acts by binding these Bmps directly and prevents their interaction with cell surface receptors (6).

We model the inhibitory effect of Noggin on the inhibitor BMP as a reaction

$$\text{BMP} + \text{Noggin} \rightarrow \varnothing,$$
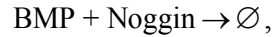
where $\varnothing$ means an inert product. Denote the rate of the reaction by $\delta(\text{Noggin})$; its effect on follicle pattern formation can be modeled as an effective rate removing the active BMP, with the turnover rate μ_R in Eq. (1) replaced by $\mu_R + \delta(\text{Noggin})$. This amounts to reducing the range of the diffusible inhibitor, X_R, via Eq. (3). To simulate the effect of Noggin treatment (Fig. 4*J*), we simply decreased X_R to some smaller values and observed the emergence of the follicles. As discussed previously, we expect this to be functionally equivalent to actually expanding the size of the grid.

SI Materials and Methods

Histology and Immunostaining.

Back skin from murine embryo was fixed in 4% paraformaldehyde, cryo-protected, embedded and sectioned at 14 μm. Primary antibodies and dilution were: rabbit anti-Atoh1(7) (1:200), goat anti-SOX2 (Neuromics, 1:600) and rabbit anti-β-galactosidase (Cappel, 1:2000).

Whole-mount X-gal staining.

Whole-mount X-gal staining for detection of β-galactosidase activity was performed as previously described(8) and the X-gal stained embryo was post-fixed in 4% paraformaldehyde. The dorsal skin was dissected out and flat-mounted for imaging by Leica MZFLIII stereo-microscope.

Skin organ culture and treatment.

E15.25 embryonic back skin explants were dissected and cultured for 24 hr on Millicell filters (Millipore) at 37°C in DMEM with 5% FCS, and 100 units/mL penicillin/ streptomycin. For experiments involving treatment of with noggin, 500 ng/mL of noggin (R&D system) was added to the culture medium.

Computational analysis

Identification of follicles and their intensities (ages).

To identify the follicles, we first transformed the 960×960 sample images in RGB color code to the single channeled Grayscale format with pixel values of intensity ranging from 0 to 255. We then performed the binarization transform through Otsu's method (9-12) to convert the Grayscale images to 0-1 matrices in which 1s represent the pixel elements that are positive of X-gal staining signals while 0s represent the non-follicle regions. To locate each individual follicle, we applied local Greedy Searching and Clustering algorithm (13) to determine the linear consecutive regions that contain follicle pixels only (locality cutoff = 4 pixels). The center of the follicle in the sample image matrix can thus be determined by calculating the average of the indices for the member pixel elements in each cluster.

Primary follicles at E15.5 day have developed the bipartite structure characterized by the expression of Sox2 in Merkel cells and the dermal papilla. We used this characteristic association with Merkel cells to identify the epithelial location of the primary hair follicles and developed a computer program tool that allows interactive manual detection and localization of primary follicles. The centers of primary follicles were labeled and recorded with respect to the Merkel cells in the sample images.

To quantify the birth time/ age of each individual follicle that has been identified, we made use of its intensity profile by staining and performed parametric fitting to a 2-dimensional Gaussian shape characterized by the Gaussian widths σ_x and σ_y and an amplitude. We performed the optimization by employing the Steepest Gradient Descent method (14) to minimize the error function of residue differences between the model and the intensity profile of

the follicle. The optimal parameters of the Gaussian model were obtained after the optimization procedure converged to the global minimum of the error function with the best fitting. The size of the follicle reflecting its observed age can thus be estimated as $\sqrt{\sigma_x^2 + \sigma_y^2}$.

Voronoi Analysis.

We employed the incremental method (15) to generate the Voronoi diagrams based on the locations of the hair follicles in $Sox2^{Ysb/+}$ and $Sox2^{Ysb/Ysb}$ samples. For instance, in order to generate the Voronoi diagram for primary follicles, we performed triangulation first on the primary anchor points following the rule of 'empty circumvent circles' (16). Therefore, the triangles with the primary follicles on the vertex nodes were optimized to have uniform and regular shapes and sizes. The bisecting lines perpendicular to the edges of these triangles were then drawn and connected to generate the dual map of the triangulation, i.e. the Voronoi diagram with the primary follicles set at the center.

Classification of secondary hair follicles.

The hair follicles that are located on the boundaries of the Voronoi diagrams of the primary follicles were classified as IIA follicles (distance to boundary less than twice of the average of diameters of non-primary follicles i.e. ~70 μm). The remaining secondary follicles were classified as IIB follicles.

The IIA hair follicles were further classified into 2 groups i.e. the vertex and the edge follicles. The criterion to make this classification is determined by the ratio of distances between the projected point of the hair follicle and the middle point of its closest edge. If the projected point is more than 1.5-fold closer to the vertex than to the middle point then it is classified as being a vertex follicle, otherwise an edge follicle, as illustrated in SI Appendix; Fig. S14.

Simulation of the EI model.

We performed the simulation of the diffusible inhibitor model defined by Eqs. (8)-(10) on a discreet lattice. Two different methods of expansion were explored. In the first, the decay length of the Green's function is decreased with time using Eq. (9). In the second, the size of the grid is gradually expanded from an initial size of 120×120 until a final size of 480×480 using

$$L(t) = L_i \cdot \left(1 + \frac{t \cdot \left(L_f - L_i \right)}{L_i \cdot T} \right),$$ (14)

where $L_i = 120$ is the initial grid size, $L_f = 480$ is the final grid size, $L(t)$ is the grid size at the current time t, and $T = 300$ is the total time of simulation. The two methods give statistically identical results (SI Appendix; Fig. S11).

At each time step, we evaluated the inhibitor concentration field $R(\bar{r},t)$ by simply summing the Green's functions (Eq. 9) for each of the current follicle locations. The initial value of l_R was chosen such that $R(\bar{r},t)$ is nowhere below the threshold, and then decreased linearly in time. At the boundaries, we have incomplete information about the inhibitor concentration, therefore we only expect accurate follicle prediction inside of a buffer region of twice l_R^*, which is the extinction length where new follicle locations are first identified. A hair follicle is generated at the global minimum of $R(\bar{r},t)$ if $R < R^*$ with $R^* = 0.1$ being a pre-specified threshold. This event is then added to the list of follicle position $\vec{r}_n$ and birth time t_n.

In case of a diffusible activator, we calculate the activator concentration as well. We used $A_0 / R_0 = 0.4$ and $X_A / X_R = 1.5$ so that the inhibitor is dominant at short scale, but the activator is longer ranged. After each step of expansion and evaluation, we searched in the grid for the positions where the R / A ratios are minimum. We generated a hair follicle at each local minimum position where $R / A < 0.1$.

To simulate the noggin treatment, we used the hair follicles present in T0 as input (Fig. 4*E*). First, we employed the EI model with the expanding mesh to generate the same number of hair follicles as those detected in controls, i.e., 40% addition of the starting number of follicles at T0 (Fig. 4*I*). We then stopped expansion and reduced the inhibitor diffusion range, to simulate the effect of noggin on BMP (see Supp Note 3). As noted above, grid expansion and inhibitor range compression are functionally identical in the EI model, thus we see that the noggin treatment leads to qualitatively similar patterns to those produced by growth alone.

Evaluation of spatial and temporal predictions by the EI model.

We selected a portion of the central area of the sample images for evaluation as follicles may be wrongly generated in the regions near the boundary of the simulation domain. We dropped a

boundary region of 50 pixels in width from the full sized area of 480x480. The boundary region is just larger than the minimum distance between primary follicles, which is 40 pixels. Thus, the domain being evaluated is 380x380 in pixel units.

The predicted follicles are paired with their nearest neighbor. Note that observed follicles can be paired with more than one predicted follicle, and this becomes more and more likely as the number of predicted follicles increases. The mean squared distance between the predicted and observed follicles, normalized by the same measurement for the null model where follicles are placed at random, is used to evaluate the strength of the EI model predictions:

$$\frac{\chi^2}{\chi^2{}_{rand}} = \frac{\left\langle \left(\vec{r}_{pred} - \vec{r}_{obs} \right)^2_{EI} \right\rangle}{\left\langle \left(\vec{r}_{pred} - \vec{r}_{obs} \right)^2_{rand} \right\rangle} . \tag{15}$$

We also use this measure to determine the robustness of the EI simulations (below).

Robustness of the results.

The relevant parameters for the EI model are the threshold value of R^* (or θ), the time step, and the grid size. We can also explore the effect of different functional forms for $G(\vec{r}|\vec{r}^*)$, which can arise from possible deviation of morphogen dynamics from the ideal diffusive behavior assumed in Eq. (9). SI Appendix; Fig. S12 shows that the EI model is remarkably robust to the choice of all these parameters and functions. This reflects the essentially geometric nature of the EI model.

We also explore the effect of initial conditions on the model predictions. The only initial condition in the model is the location of primary follicles. Occasionally, smaller primary follicles are misidentified as secondary follicles. To investigate the effect of such an error, we randomly change some identified primary follicles to secondary follicles in one pattern. SI Appendix; Fig. S13*A* shows the positional error in the predicted follicles given different numbers of primary follicles (legend). The error in the predictions increases very gradually at first, but becomes more severe when 20% of the primary follicles are misidentified. SI Appendix; Fig. S13*B* shows that the errors in the predicted follicle locations are localized to a region directly surrounding the missing follicle. Additionally, in many cases, the EI model correctly places a secondary follicle very near the missing primary follicle. We conclude that the EI model predictions are remarkably

robust to error in the initial conditions as well.

Supplementary references

1. Headon, D. J. & Painter, K. J. (2009) Stippling the skin: Generation of anatomical periodicity by reaction-diffusion mechanisms. *Math. Model. Nat. Phenom.* **4**, 83-102.

2. Turing, A. M. (1952) The Chemical Basis of Morphogenesis. *Philos. Trans. R. Soc. London B Biol. Sci.* **237**, 37-72.

3. Gierer, A. & Meinhardt, H. (1972) A theory of biological pattern formation. *Biol. Cybern.* **12**, 30-39.

4. Chang, C. & Hemmati-Brivanlou, A. (1999) Xenopus GDF6, a new antagonist of noggin and a partner of BMPs. *Development* **126**, 3347-3357.

5. Merino, R., Macias, D., Ga+¦an, Y., Economides, A. N., Wang, X., Wu, Q., Stahl, N., Sampath, K. T., Varona, P., & Hurle, J. M. (1999) Expression and Function of Gdf-5 during Digit Skeletogenesis in the Embryonic Chick Leg Bud. *Developmental Biology* **206**, 33-45.

6. Zimmerman, L. B., De Jes·s-Escobar, J. M., & Harland, R. M. (1996) The Spemann Organizer Signal noggin Binds and Inactivates Bone Morphogenetic Protein 4. *Cell* **86**, 599-606.

7. Helms, A. W. & Johnson, J. E. (1998) Progenitors of dorsal commissural interneurons are defined by MATH1 expression. *Development* **125**, 919-928.

8. Leung, K. K. H., Ng, L. J., Ho, K. K. Y., Tam, P. P. L., & Cheah, K. S. E. (1998) Different cis-Regulatory DNA Elements Mediate Developmental Stage- and Tissue-specific Expression of the Human COL2A1 Gene in Transgenic Mice. *J. Cell Biol.* **141**, 1291-1300.

9. Baltus, A. E., Menke, D. B., Hu, Y. C., Goodheart, M. L., Carpenter, A. E., de Rooij, D. G., & Page, D. C. (2006) In germ cells of mouse embryonic ovaries, the decision to enter meiosis precedes premeiotic DNA replication. *Nat. Genet.* **38**, 1430-1434.

10. Otsu, N. (1979) A threshold selection method from gray level histograms. *IEEE Trans. Sys. , Man. , Cyber.* **9**, 62-66.

11. Lutes, A. A., Neaves, W. B., Baumann, D. P., Wiegraebe, W., & Baumann, P. (2010) Sister chromosome pairing maintains heterozygosity in parthenogenetic lizards. *Nature* **464**, 283-286.

12. Wang, Y., Botvinick, E. L., Zhao, Y., Berns, M. W., Usami, S., Tsien, R. Y., & Chien, S. (2005) Visualizing the mechanical activation of Src. *Nature* **434**, 1040-1045.

13. Gdalyahu, Y., Weinshall, D., & Werman, M. (2001) Self-organization in vision: Stochastic Clustering for Image Segmentation, Perceptual Grouping and Image Database Organization. *IEEE Trans. on Pattern Analysis and Machine Intelligence* **23**, 1053-1074.

14. Nocedal, J. & Wright, S. J. (2006) *Numerical Optimization* (Springer-Verlag, Berlin, New York).

15. Hjelle, O. & Daehlen, M. (2006) (Springer, Berlin Heidelberg), pp. 1-21.

16. Okabe, A., Boots, B., Sugihara, K., Chiu, S. N., & Kendall, D. G. (2000) in *Spatial Tessellations* (John Wiley & Sons, Inc., pp. 43-112.

17. Sick, S., Reinker, S., Timmer, J., & Schlake, T. (2006) WNT and DKK Determine Hair Follicle Spacing Through a Reaction-Diffusion Mechanism. *Science* **314**, 1447-1450.
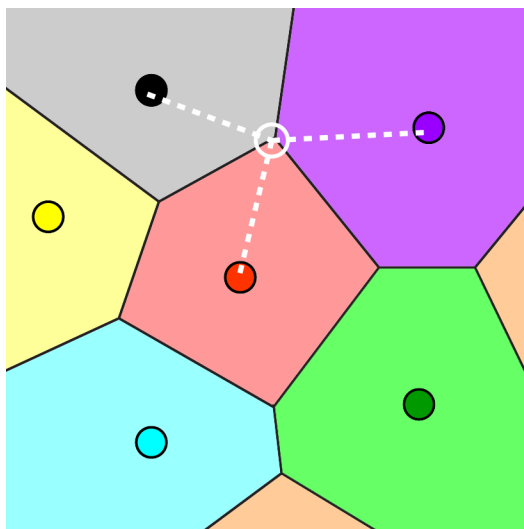
Fig. S1: Voronoi analysis. Voronoi tessellation is mathematical method widely used in the analysis of spatial structures (13). Given a set of N anchor points in 2-dimensional space, a Voronoi diagram is generated by subdividing the space into N non-overlapping polygons (called the "Voronoi cells") such that all points inside a cell have the shortest distances to the anchor point of that cell than any other anchor points. In the above figure, the anchor points are the colored circles, and the Voronoi cells are the colored regions bordered by the black lines (called the "Voronoi edges"). All points inside a colored region are closer to the circle of the same color than to any other circles. A property of the Voronoi cells important for the present study is that a Voronoi vertex, defined by the intersection of typically 3 Voronoi edges and illustrated by a white open circle, is at an equal distance from the three surrounding anchor points (white dash lines), and any points in the vicinity of the vertex will be closer to at least one of the anchor points.
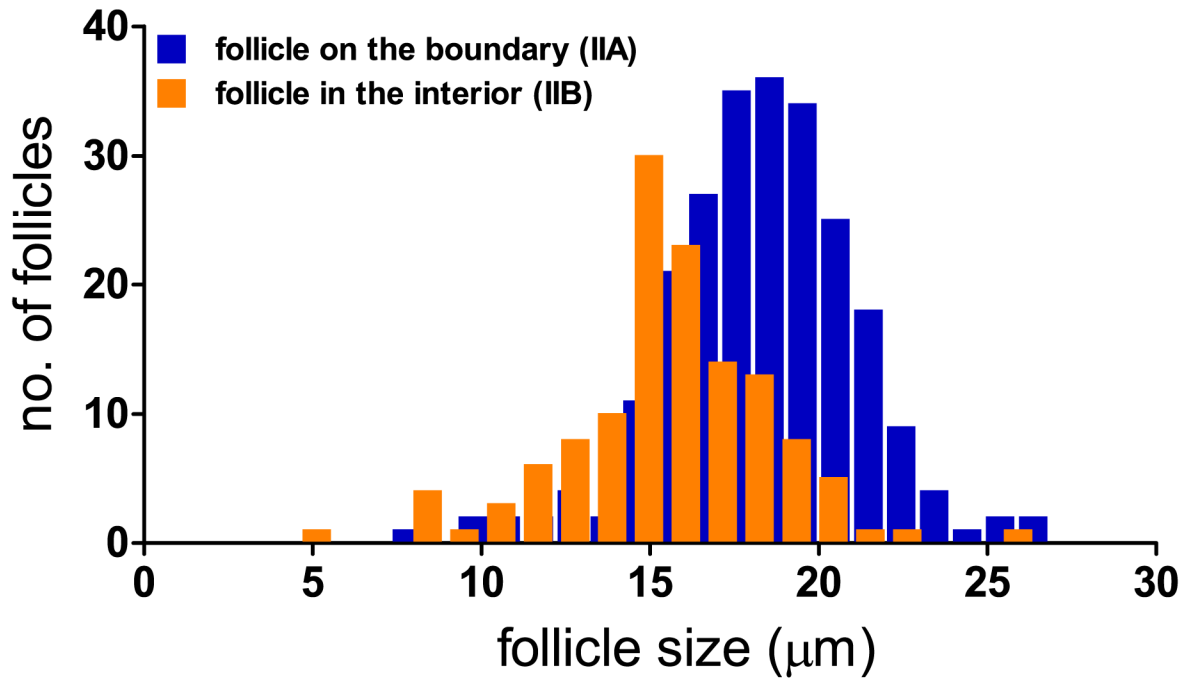
Fig. S2: Follicles located in the interior of Voronoi cells have younger ages than follicles at the boundary. We assume the size of the follicles reflect their ages and analyzed the follicle sizes. The spatial distribution of X-gal stain intensity of each identified secondary follicle is fitted to a 2-dimensional Gaussian function parameterized by two widths, σ_x and σ_y, and the "size" of the follicle is defined as $\sqrt{\sigma_x^2 + \sigma_y^2}$; see *SI Materials and Methods* Computational analysis for details. Data were collected for the secondary follicles on the E15.5 skins and sorted into two groups, according to whether they are located on the boundaries (IIA) or in the interior space (IIB) of the Voronoi cells generated from the primary follicles; see Fig. 1*G*. Size distribution of the IIA (blue) and IIB (orange) follicles show that the average size of the IIA follicles is 18.3 µm and the IIB follicles is 15.6 µm (n=3). Thus, we expect the IIA follicles to form somewhat than the IIB follicles. However, this temporal order is not expected to be very sharp according to the simulation result of SI Appendix; Fig. S4, thus explaining the substantial overlap of the two distributions.
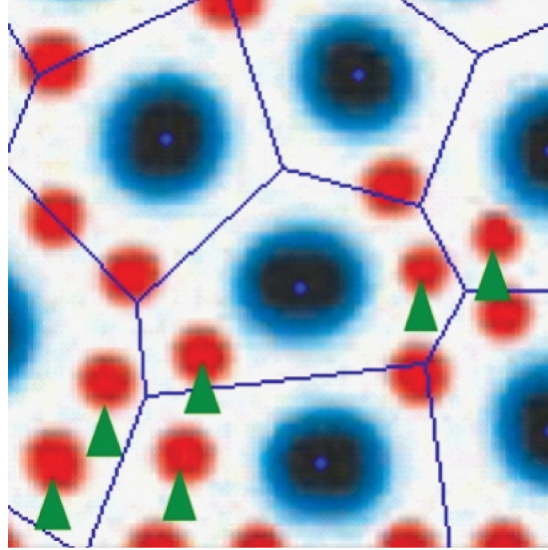
Fig. S3: Voronoi analysis of the computational result of Sick et al (17). In Ref(17), two waves of hair follicles were generated by first using a Turing RD model to generate the primary follicles, followed by a spatial expansion, and another round of RD model to generate the secondary follicles in the interstitial space of the primary follicles (which are held fixed in the study once generated by the first RD run). Clearly, the secondary follicles generated this way all appear around the same time instead of the sequential appearance predicted by the EI model. The spatial positions of the newly generated follicles are also different from those of the EI model. The figure above shows the predictions of Sick *et al*'s model, with the blue and red dots being the primary and secondary follicles respectively, superimposed with the Voronoi cells generated from the primary follicles. While many follicles fall on the Voronoi boundaries, there are also substantial numbers of follicles that do not adhere to the Voronoi boundaries. For example, in the regions indicated by the green arrows, the red follicles essentially fill up the open space with a preferred spacing without regard to the Voronoi boundaries. Moreover, the preferred spacing is highly parameter dependent, such that denser filling of the interstitual space can be easily arranged by, e.g., reducing the scale of the diffusion zone (ℓ). Thus, the patterns generated by the Turing RD model are sensitively dependent on the model parameters.
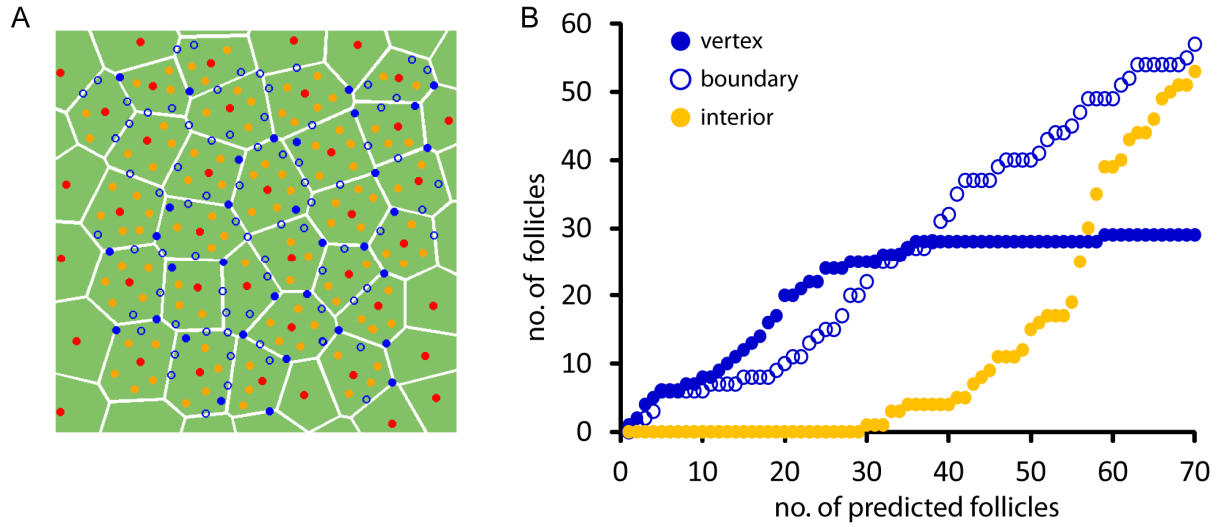
Fig. S4: Positions of the inserted secondary follicles. (*A*) Follicles generated by the EI model are classified into one of the three types according to their positions close to the vertices (solid blue), edges (open blue), and the interiors (orange) of the Voronoi cells generated according to the positions of the primary follicles (red). (*B*) The total number of each of these classes of new follicles is plotted against the total number of predicted follicles. Initially, the there is a preference for the follicles to occupy the vertices (solid blue), with also a substantial number of edge positions (open blue). After around 30 predicted follicles, the vertex positions become mostly occupied and follicles formed after that started to take on interior positions (orange.)
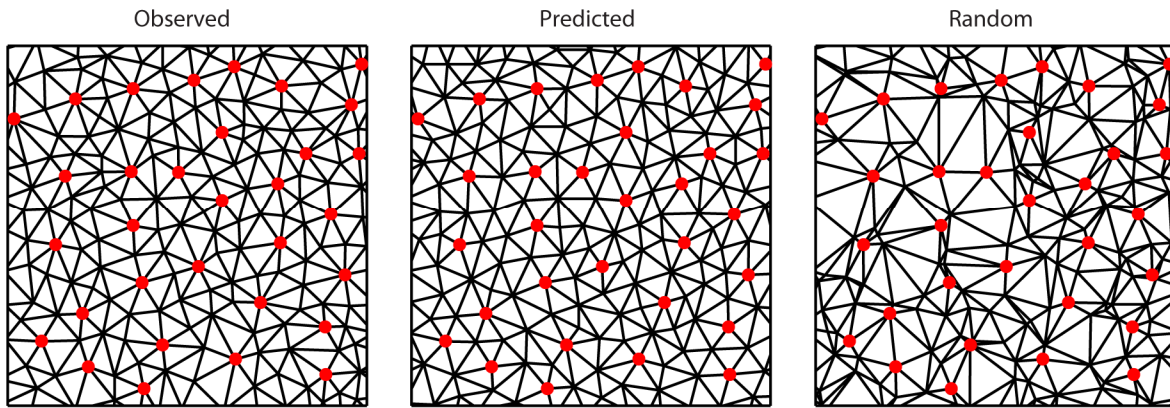
Fig. S5: The EI model reproduces the regularity of neighboring follicle distances in the skin. The locations of observed primary follicles plus observed secondary follicles *(left)*, EI predicted secondary follicles *(middle)*, or random secondary follicles *(right)*, are used to construct Delaunay triangulations, where lines connect all neighboring follicles. Primary follicles in each case are indicated with red dots. The distribution of distances between all nearest neighbor pairs is computed from this pattern, and is observed to be sharply peaked in the observed and predicted patterns (Fig. 3*C*). The Delaunay triangulation also reveals the regularity in the observed and predicted follicle patterns that is not evident in the random pattern.
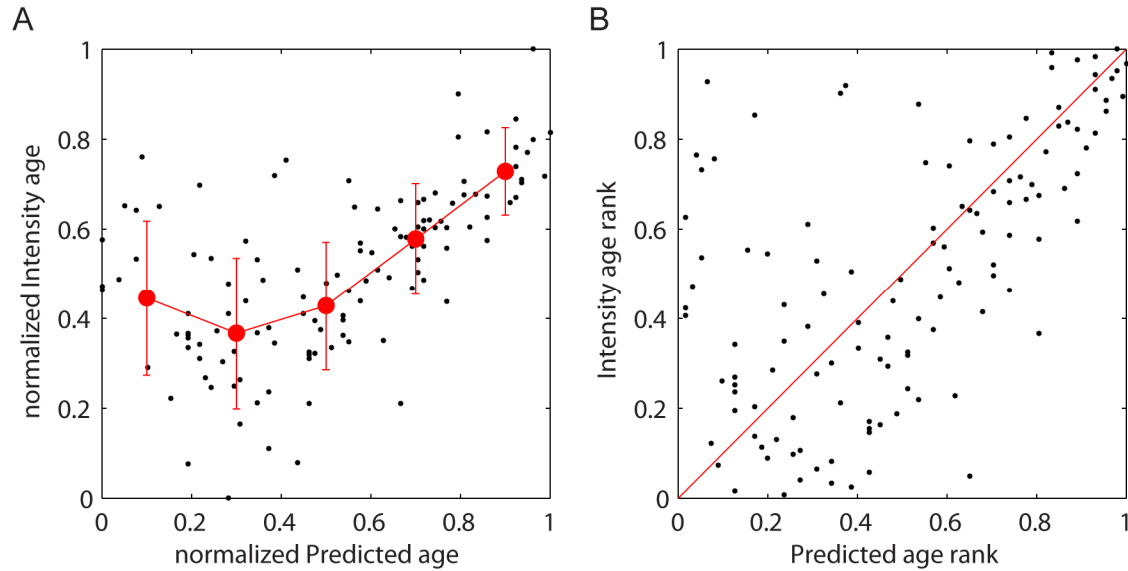
Fig. S6: Calculating the density from the rank plot of the observed age vs. the EI predicted age. *(A)* The intensity age of secondary follicles is plotted versus the EI predicted age for a representative sample of *Sox2*^{Ysb/+} skin. The observed and predicted ages are clearly correlated for the oldest follicle; however, the correlation weakens for the younger (more lightly stained) follicles, due presumably to the staining characteristics (SI Appendix; Fig. S7), and differs from one image to another. *(B)* The rank plot for the same data in *(A)* shows that there is still significant noise, but the distribution is centered along the diagonal. The rank is normalized by the number of follicles observed, permitting all samples to be plotted together (as in Fig. 3*D*) and improving the statistics of the timing correlation. The density heat plot from Fig. 3*D* is calculated by 2D binning of the combined rank plot for all skin samples: we count the points in each of 10x10 bins in both directions.
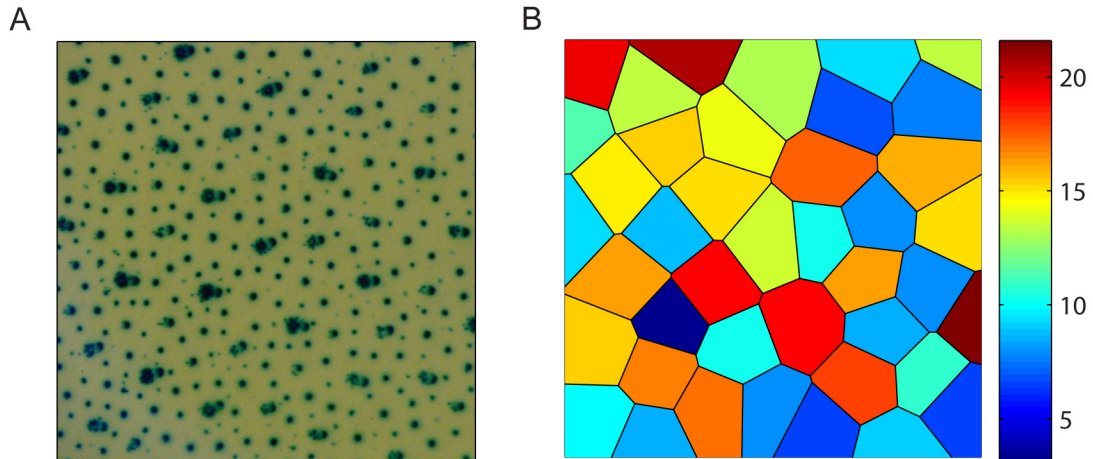
Fig. S7: The noise in the follicle age is due to heterogeneity in follicle staining.

(A) A representative image from the *Sox2$^{Ysb/Ysb}$* E15.5 skins shows that there is significant variation in the follicle staining intensities, which could be due to staining or image efficiency, or other effects not accounted for in our model. *(B)* This variation can be seen even in the intensity of the primary follicles. We plot the Voronoi diagram for the primary follicles in *(A)*, with the color representing the integrated intensity of each central primary follicle. The ~50% variation in the primary follicle intensity is similar to that of the secondary follicles and the two are not correlated (not shown).
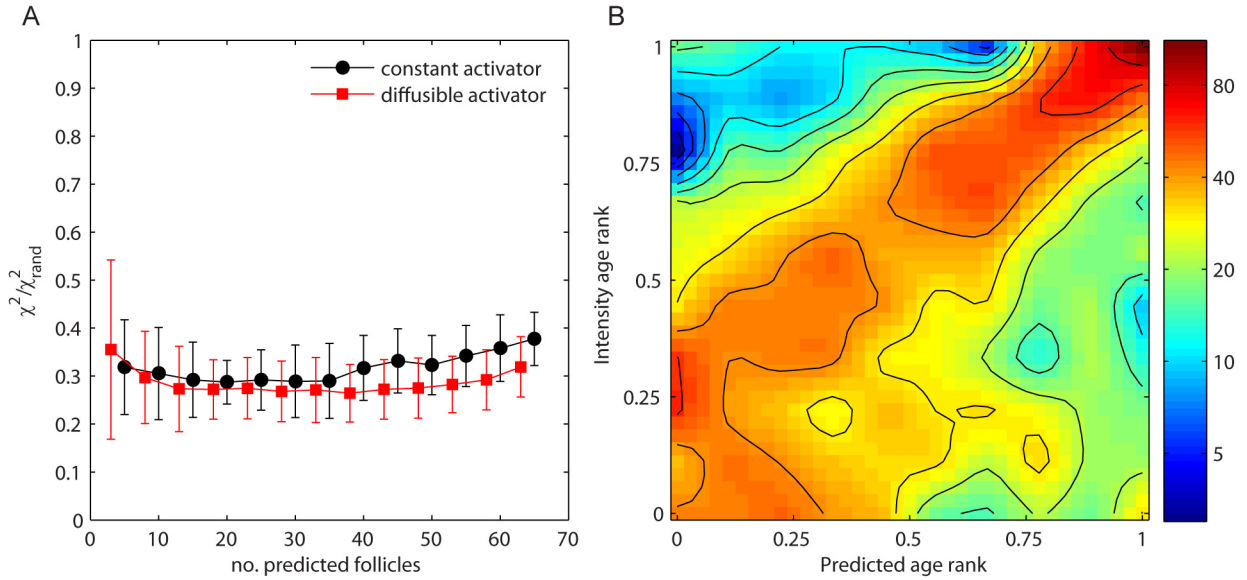
Fig. S8: **The EI models with diffusible activator (red square) and basal activator (black circle) showed similar performances in predicting the process of spatial-temporal patterning of secondary hair follicles in *Sox2^Ysb/+*** samples (n=10).** The Expansion-Induction model can explain the spatial patterns (*A*) and timing (*B*) of the secondary follicles using either a constant basal activation (black circles as in Fig. 3*B*) or a diffusible activator synthesized from the follicles (red squares). This rule holds as long as i) the activators diffuses to a longer range than the inhibitors and ii) the new hair follicles produce morphogens (activators and inhibitors) at the same rate as the existing follicles. See *SI Materials and Methods* for the details of the simulation.
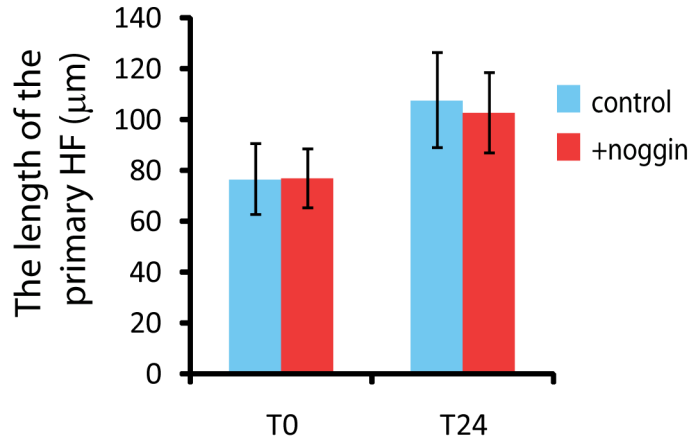
Fig. S9: Increase in vertical length of the primary hair follicle in explant culture. In explant culture experiments, the length of the hair follicles is increased after 24 hours culture, indicating the viability of the explant.
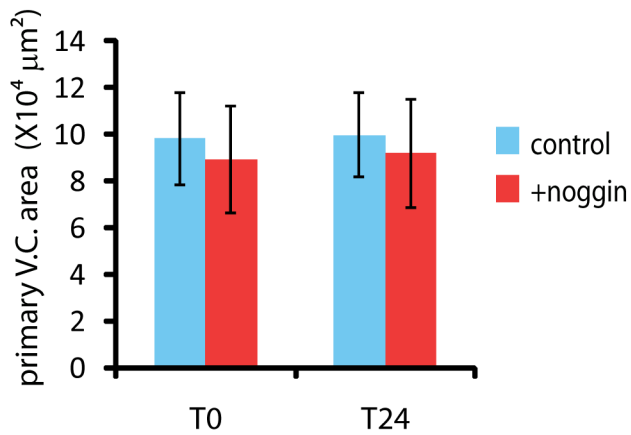

Fig. S10: No significant lateral growth of the explant during culture. The average area of the Voronoi cells generated by the primary hair follicles at the beginning of culture (T0) and after 24 hours incubation (T24). There is no significant difference between the area at T0 and T24 in both control and noggin treated samples, and suggests that is no significant lateral growth of the explant culture.
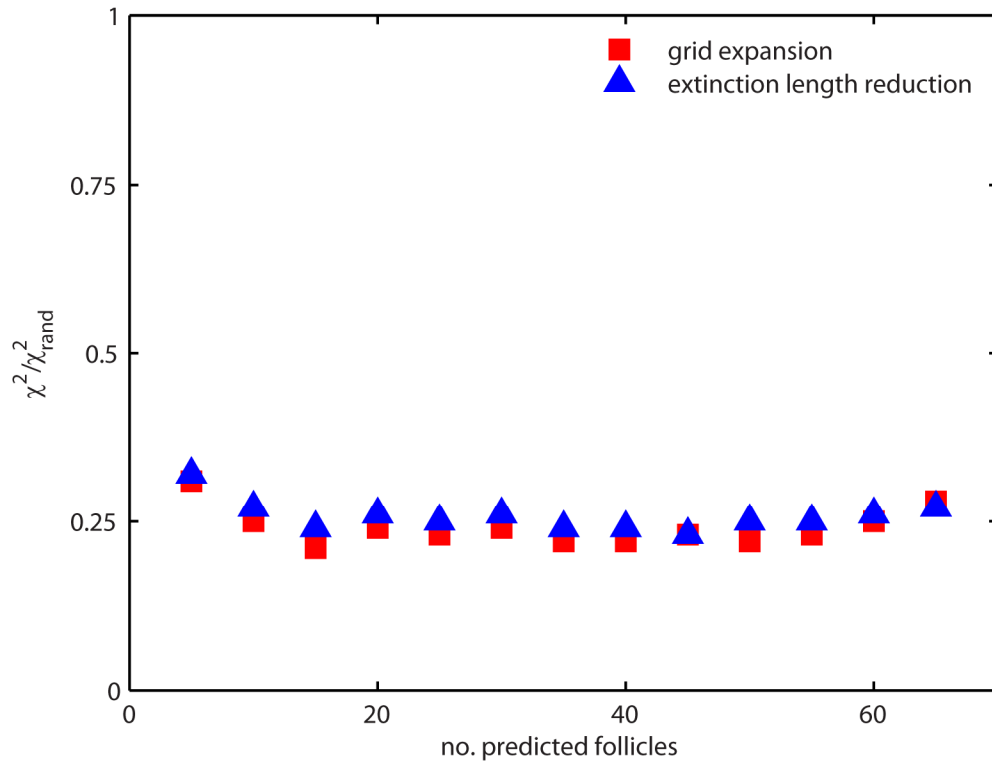
Fig. S11: Reducing the extinction coefficient of the Green's function with time is functionally equivalent to expanding the grid. The positional error of the EI predictions are plotted for a simulation using grid expansion to induce follicle formation (red), and a simulation where the follicle induction is produced by decreasing the extinction length of the Green's function with time (blue). The same primary follicle pattern is used for both simulations, and the methods produce the same accuracy of predictions. This explains why qualitatively identical follicle patterns are produced for the $Sox2^{Ysb/+}$ and the $Sox2^{Ysb/Ysb}$ skins, where follicles are induced through growth and expansion, and with noggin treated skins, where induction is assumed to result from reducing the length scale of inhibitors.
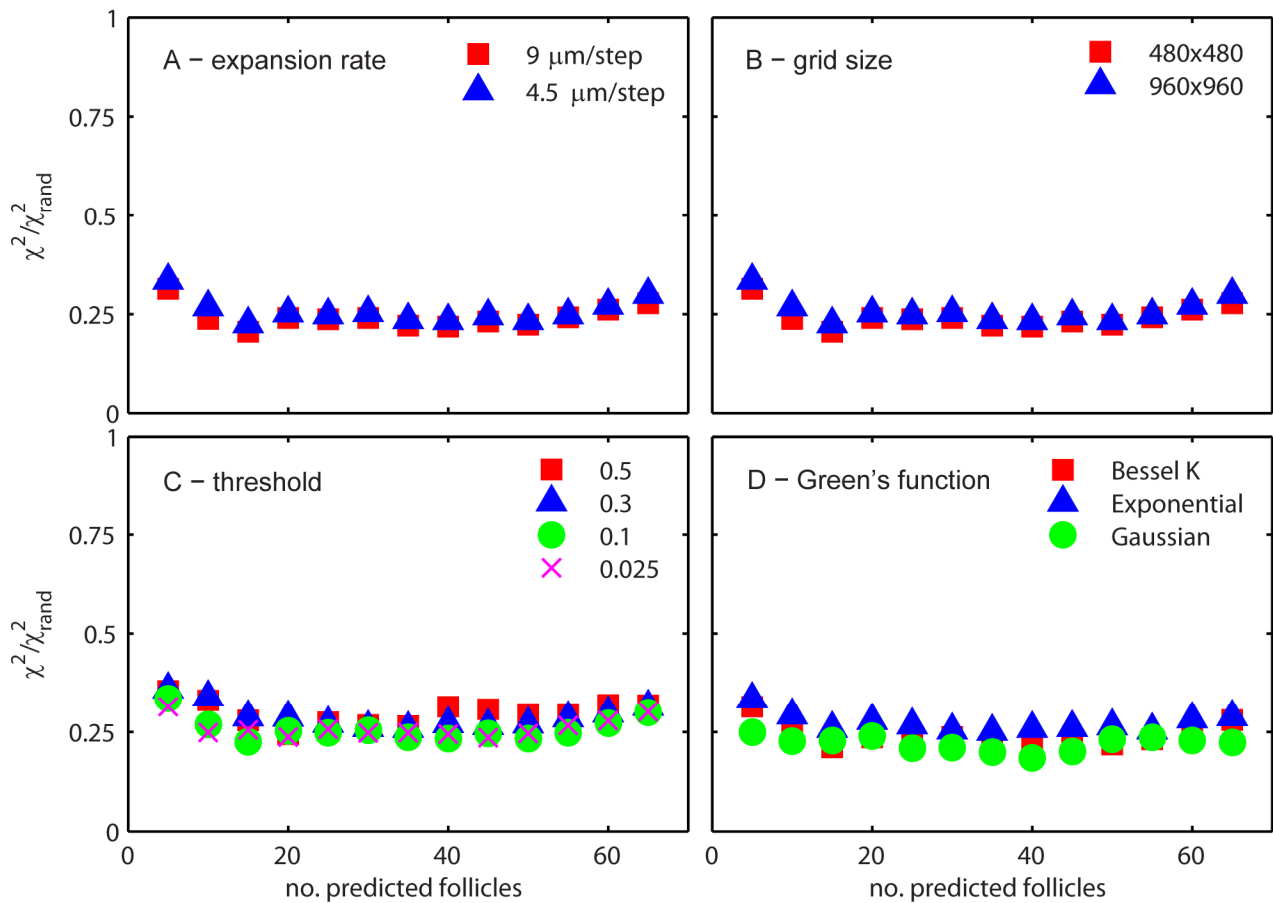
Fig. S12: The EI model predictions are robust to parameter changes. In each panel, the positional error in the predicted follicles is plotted vs. the number of predicted follicles for a representative *Sox2^{Ysb/+}* E15.5 skin. The predictions are remarkably robust to changes in all of the relevant simulation parameters. In these simulations, expansion is accomplished through gradual reduction of the extinction length in the Green's function rather than expansion of the grid. In *(A)* we vary the expansion rate. The expansion rate determines the time scale (*see SI Materials and Methods*); therefore, this is equivalent to changing the time step. *(B)* The resolution of the image is changed two-fold. This changes the minimum length scale in the simulation. In *(C)* we vary the threshold level (dimensionless units), and in *(D)* we use different functional forms of the Green's function.
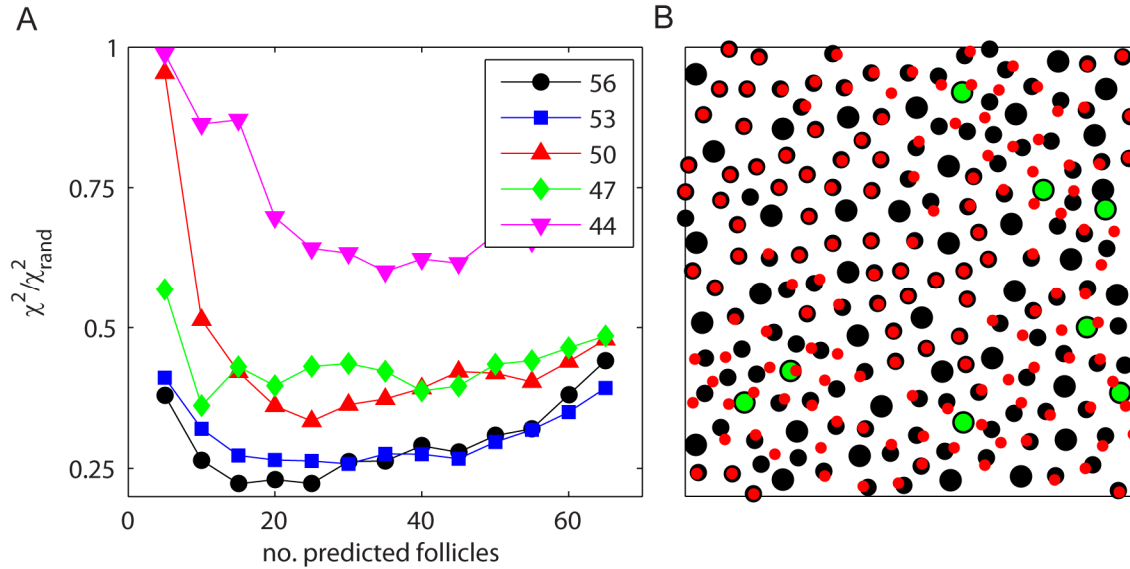
Fig. S13: Errors in initial conditions decrease the accuracy of predictions in a smooth manner. *(A)* The primary follicle locations are the only initial condition to the EI model. The most common problem with determining the initial condition is the misidentification of smaller primary follicles as secondary follicles. We investigate the effect of this misidentification by randomly identifying some primary follicles as secondary follicles. The positional error in the predictions is plotted versus the number of follicles predicted for different numbers of primary follicles in the initial condition (legend). The error changes smoothly with primary follicle number until 20% of the follicles are removed. *(B)* The positional error in the predicted pattern is localized to the region where the initial condition is missing. In this plot, the positions of the primary follicles are depicted by large black circles. Predicted secondary follicles using the complete set of primary follicles are plotted as smaller black dots. The green circles indicate primary follicles that have been removed from the initial condition in the second simulation, and red dots show the new predicted follicle locations.
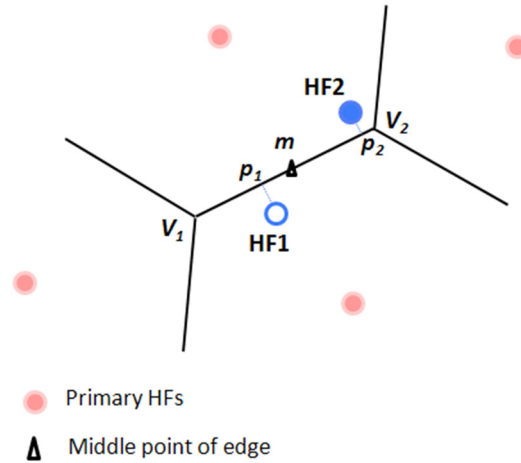
Primary HFs

Middle point of edge

Fig. S14: Identifying the position classes of the secondary follicles. The black lines are the edges of the Voronoi diagram generated based on the positions of the primary follicles (red circles). HF_1 and HF_2 (blue circles) are two secondary follicles. p_1 and p_2 are their projections onto the closest edge $\overline{v_1 v_2}$. m is the middle point of this edge. Since the ratio of distances $d(p_1,m)/d(p_1,v_1)$ is less than 1.5-fold, HF_1 is classified as a hair follicle on the edge while HF_2 is classified as a vertex HF because $d(p_2,m)/d(p_2,v_2)$ is greater than 1.5-fold.